MATERIALS CHEMISTRY
FRONTIERS

CHINESE CHEMICAL SOCIETY

ROYAL SOCIETY OF CHEMISTRY

RESEARCH ARTICLE

View Article Online
View Journal | View Issue

Cite this: *Mater. Chem. Front.*, 2020, **4**, 1656

Polydopamine sacrificial layer mediated SiO_x/C@C yolk@shell structure for durable lithium storage†

Yuanyuan Zhang, Guangwu Hu, Qiang Yu, Zhenhui Liu,* Chang Yu, Longsheng Wu, Liang Zhou* and Liqiang Mai

Received 2nd March 2020,
Accepted 20th April 2020

DOI: 10.1039/d0qm00120a

rsc.li/frontiers-materials

SiO_x has aroused great attention as a lithium-ion battery anode material owing to its lower cost and smaller volume expansion than Si. Nevertheless, its practical application is hindered by the still existing volume expansion and low electrical conductivity, resulting in rapid capacity decay. Herein, SiO_x/C@N-doped carbon yolk@shell microspheres (denoted as YS-SiO_x/C@C) have been constructed by a polydopamine-mediated selective etching strategy. In the constructed material, a SiO_x/C composite core is encapsulated in a N-doped hollow carbon sphere with sufficient void space existing between the SiO_x/C core and carbon shell. The yolk@shell structure could buffer the large volume fluctuation, resulting in significantly enhanced structural stability. Benefiting from the structural merits, the new composite delivers a stable high capacity of 804 mA h g^{-1} at 100 mA g^{-1} and long-term cyclability (1000 cycles at 500 mA g^{-1}). Besides, the HF-free polydopamine-mediated selective etching strategy developed here paves a new way to construct yolk@shell structures for electrode materials.

Introduction

Driven by the rapid development of portable electronics and electric vehicles, the demands on the energy density of lithium-ion batteries (LIBs) are ever increasing.[1,2] Si is a promising candidate anode material to replace commercial graphite owing to the abundant resource, suitable Li-uptake potential, and ultrahigh theoretical capacity.[3–6] However, the huge volume fluctuation (around 400%) of Si may lead to solid electrolyte interface (SEI) rupture, active material pulverization, and active material peeling off from current collectors, eventually resulting in rapid capacity fading.[7–9] Fabricating Si nanoparticles and nanostructures can alleviate the volume variation issue.[10–13] However, the production cost of such Si nanoparticles and nanostructures is pretty high, although raw Si is very cheap. Both factors frustrate the practical application of Si in commercial LIBs.

Recently, nonstoichiometric SiO_x ($0 < x < 2$) has demonstrated fascinating research value due to its lower production cost and smaller volume expansion compared to Si.[14–18] The *in situ* formed Li_2O and lithium silicates may alleviate the volume fluctuation during subsequent lithiation/de-lithiation processes and help build up a stable SEI layer.[18–20] Nevertheless, large volume variation still exists for SiO_x and its intrinsic electrical conductivity is unsatisfactory, resulting in inferior cycle life and rate performance. These issues should be addressed before commercialization.

Yolk@shell composites with well-developed voids in between the yolk and shell demonstrate unique merits in addressing the volume change bottleneck of anode materials.[21–26] A series of yolk@shell structured anode materials have been designed recently, including Si@C,[27] Sb@C,[28] Sn@C,[29] and FeO_x@C.[30] In these composites, the hollow cavity in between the outer shell and inner core is able to buffer the volume fluctuation of high-capacity anode materials. Meanwhile, the carbon shell affords high conductivity and enhanced structural stability. However, yolk@shell structures with a SiO_x-based inner core and carbon shell have not been reported yet.

Herein, we report a polydopamine-mediated selective etching strategy to construct SiO_x/C@N-doped carbon yolk@shell microspheres (YS-SiO_x/C@C). The resultant YS-SiO_x/C@C composite delivers high capacity with durable cyclability and ideal rate capability. Specifically, the obtained YS-SiO_x/C@C displays a high and stable capacity of 804 mA h g^{-1} at 100 mA g^{-1}. Considering that dopamine can be coated onto the surface of various materials, it is anticipated that the HF-free polydopamine-mediated selective etching strategy introduced in this work might be generalized to the construction of other yolk@shell structures when the core materials are resistant to NaOH etching.

State Key Laboratory of Advanced Technology for Materials Synthesis and Processing, Wuhan University of Technology, Wuhan 430070, P. R. China. E-mail: liuzhenhui0328@whut.edu.cn, liangzhou@whut.edu.cn

† Electronic Supplementary Information (ESI) available: XRD patterns, Raman spectra, FT-IR spectra, EIS plots and cycling performance. See DOI: 10.1039/d0qm00120a

Experimental

Preparation of organosilica materials

For the synthesis of organosilica microspheres, aqueous ammonia (NH_4OH, 25 wt%, 1 mL) was added to 50 mL of water. Afterwards, 1 mL of vinyltrimethoxysilane (VTMS) was introduced. After continuous reaction for 6 hours at 25 °C, the mixture was centrifuged and washed with water, and the organosilica microspheres were collected after drying.

Preparation of organosilica@PDA microspheres

The organosilica microspheres were dispersed in 75 mL Tris–HCl buffer. Subsequently, 300 mg of dopamine hydrochloride was introduced. The organosilica@polydopamine (organosilica@PDA) microspheres could be collected after centrifugation and drying. (Tris–HCl buffer solution was obtained by adding 0.8 g Tris and 0.12 mL concentrated hydrochloric acid in 150 mL H_2O, ensuring that the pH was around 8.)

Preparation of organosilica@PDA@PPy

The organosilica@PDA microspheres were dispersed in 60 mL H_2O. Then, 75 μL pyrrole monomer, 12 mg sodium dodecyl sulfate and ammonium persulphate solution (180 mg in 5 mL H_2O) were sequentially added to the suspension. After stirring for 12 h, organosilica@PDA@polypyrrole (organosilica@PDA@PPy) was obtained after centrifugation and washing.

Preparation of organosilica@void@PPy materials

The obtained organosilica@PDA@PPy microspheres were dispersed in 100 mL H_2O. Then, 100 mg NaOH was introduced into the suspension. After stirring at 70 °C for 5 hours, the mixture was centrifuged and washed with water until the pH reached neutral, and the yolk@shell organosilica@void@PPy microspheres were obtained after freeze-drying.

Preparation of YS-SiO_x/C@C

To obtain the final YS-SiO_x/C@C, the as-synthesized organosilica@void@PPy microspheres were annealed in Ar at 800 °C for 5 hours. For comparison, SiO_x/C microspheres were synthesized from organosilica microspheres through the same annealing process.

Material characterization

Scanning electron microscopy (SEM) images were obtained on a JEOL-7100F microscope. Transmission electron microscopy (TEM) images, high-resolution TEM (HRTEM) images, and energy dispersive X-ray spectroscopy (EDS) elemental mapping were collected on a JEM-2100F microscope. X-ray diffraction (XRD) patterns were recorded using a Bruker D8 Advance X-ray diffractometer with a non-monochromated Cu Kα X-ray source (λ = 1.5418 Å). X-ray photoelectron spectroscopy (XPS) spectra were obtained on a VG Multilab 2000 X-ray photoelectron instrument. Raman spectra were recorded with a micro-Raman spectroscopy system (Renishaw INVIA) with an Ar 514.5 nm laser. The Brunauer–Emmett–Teller (BET) surface areas were calculated from N_2 sorption results, which were measured on a Tristar-3020 instrument at 77 K. Fourier-transform infrared spectroscopy (FT-IR) spectra were performed by a Spectrum One Infrared 134 spectrometer. The carbon content was obtained using thermogravimetric analysis (TGA) (NETZSCH STA 449F5) apparatus, and the samples were heated to 900 °C in air with a heating rate of 10 °C min^{-1}.

Electrochemical characterization

The active material (70 wt%), acetylene black (20 wt%), and sodium alginate (10 wt%) were dispersed in water to form a slurry. The slurry was spread onto copper foil by the doctor blade method. The mass loading of the active material was 1.0–1.5 mg cm^{-2}. The electrolyte was 1.0 M $LiPF_6$ in ethylene carbonate/dimethyl carbonate (1 : 1 by volume) containing 5 vol% fluoroethylene carbonate (FEC). A Whatman glass fiber membrane (GF/A) was used as the separator. Li foil was used as the reference electrode in half cells. Discharge/charge measurements were performed in a potential window of 0.01–2.0 V (*vs.* Li^+/Li) using a Neware CT4008 battery testing system. Cyclic voltammetry (CV) was performed with

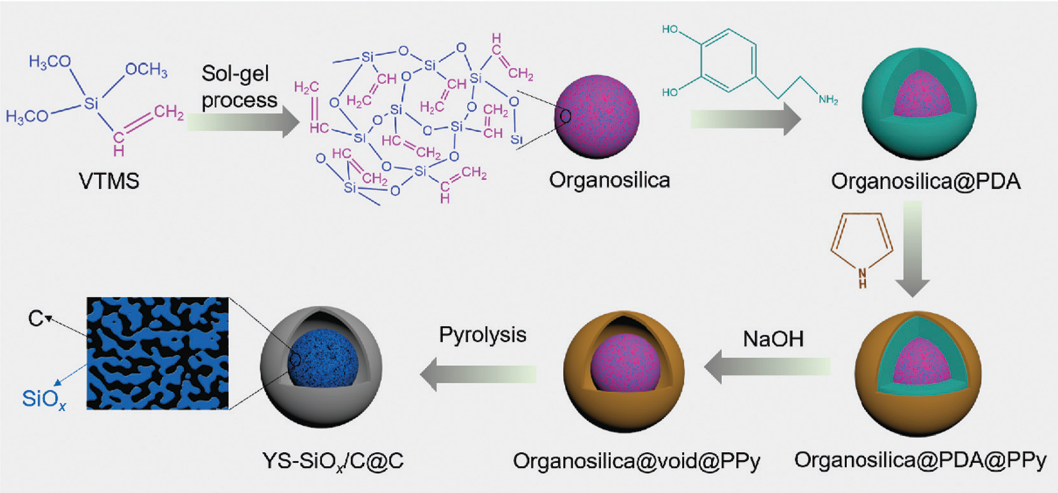

Fig. 1 Schematic illustration of the construction of YS-SiO_x/C@C composites.

an Autolab PGSTAT 302N electrochemical workstation. Electrochemical impedance spectra (EIS) were conducted in the frequency range of 100 kHz to 0.1 Hz.

The YS-SiO_x/C@C//$LiFePO_4$ full cells were assembled with a cathode material/anode material ratio of about 4 : 1. 1.0 M $LiPF_6$ in ethylene carbon/dimethyl carbonate/ethyl methyl carbonate (1 : 1 : 1 by volume) was used as the electrolyte and Celgard-2400 was used as the separator. Before full cell assembly, the YS-SiO_x/C@C composite was pre-lithiated in half cells. The YS-SiO_x/C@C//$LiFePO_4$ full cells were cycled at 0.1C (1C = 170 mA g^{-1}) in a voltage window of 2.2–4.0 V.

Results and discussion

The YS-SiO_x/C@C microspheres were prepared through a polydopamine-mediated selective etching strategy (Fig. 1). First, organosilica microspheres were prepared through the sol–gel method using VTMS as the precursor. Afterwards, polydopamine (PDA) and polypyrrole (PPy) were coated onto VTMS-derived organosilica in sequence, and three-layer structured organosilica@PDA@PPy microspheres were obtained. Compared to organosilica and PPy, PDA shows weaker etching resistance in alkaline medium.[31,32] As a result, the PDA sacrificial layer in the three-layer structured organosilica@PDA@PPy microspheres can be selectively removed in aqueous NaOH solution, and yolk@shell structured organosilica@void@PPy microspheres can be obtained. When annealed in Ar, the organic groups in organosilica and PPy were converted into amorphous carbon, and YS-SiO_x/C@C microspheres were obtained. It should be mentioned that dopamine has been widely studied as a coating material to construct core@shell structured materials.[33] Its polymerization can lead to uniform polydopamine coatings or carbon coatings after carbonization. In this study, we employ polydopamine as a sacrificial layer for the construction of yolk@shell structures.

The organosilica microspheres show a well-defined spherical morphology with uniform diameters of approximately 300 nm (Fig. 2a and d). After coating with PDA, a uniform and conformal layer can be observed on the surface of organosilica (Fig. 2b and e). The thickness of the PDA layer is ~25 nm (Fig. 2e). After the subsequent PPy coating step, an additional PPy coating layer with a thickness of ~30 nm can be discerned on the surface (Fig. 2c and f). The average size of organosilica@PDA@PPy reaches 400 nm, much larger than that of the original organosilica spheres.

The PDA intermediate layer of the three-layer structured organosilica@PDA@PPy can be selectively etched by NaOH and YS-SiO_x/C can be obtained after further high temperature treatment in Ar. The morphology features of the obtained YS-SiO_x/C@C are characterized by SEM and TEM (Fig. 3). A well-defined yolk@shell structure can be discerned in Fig. 3a–c. The yolk is composed of SiO_x/C, and it has a size of ~250 nm, slightly smaller than the size of the organosilica precursor due to the corrosion of NaOH.[34] The shell is composed of PPy derived N-doped carbon and it has a thickness of ~30 nm, which is similar to the thickness of the PPy layer. Between the SiO_x/C yolk and carbon shell, there is a large hollow cavity which is caused by the NaOH etching process. It is expected that the hollow cavity can accommodate the large volume fluctuation of SiO_x/C and thus boost its cyclability. EDS mapping shows that C and N distribute homogeneously all over the whole particle, whereas Si and O mainly distribute at the yolk area and their signals overlap with each other, clearly demonstrating the SiO_x/C@C yolk@shell structure of the product (Fig. 3d–i).

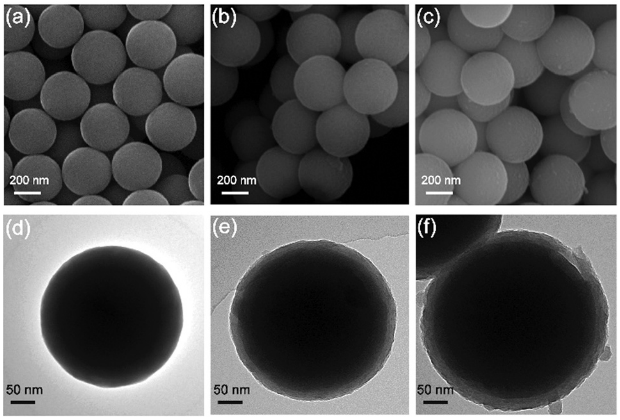

Fig. 2 SEM images of organosilica (a), organosilica@PDA (b) and organosilica@PDA@PPy (c); TEM images of organosilica (d), organosilica@PDA (e) and organosilica@PDA@PPy (f).

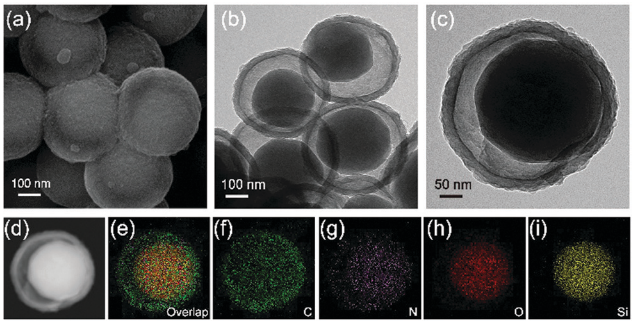

Fig. 3 SEM (a) and TEM (b and c) images of YS-SiO_x/C@C, and the high-angle annular dark field (HAADF) image (d) and its corresponding EDS mapping images (e–i).

Fig. S1 (ESI†) presents XRD patterns of SiO_x/C and YS-SiO_x/C@C. The broad diffraction located at 2θ = 20–25° is associated with amorphous non-stoichiometric SiO_x and carbon.[35] The graphitization degree of carbon is examined using Raman spectra (Fig. S2, ESI†). The peaks located at 1335 cm^{-1} and 1607 cm^{-1} can be assigned to the D band and G band, respectively.[36] YS-SiO_x/C@C displays a higher I_G/I_D ratio than SiO_x/C, demonstrating the higher graphitization degree of the N-doped carbon shell derived from PPy.

The carbon content of the composite materials is analyzed by TGA (Fig. 4a). YS-SiO_x/C@C shows a higher carbon content and lower thermolysis temperature than SiO_x/C on account of the existence of N doping in carbon. The carbon content for

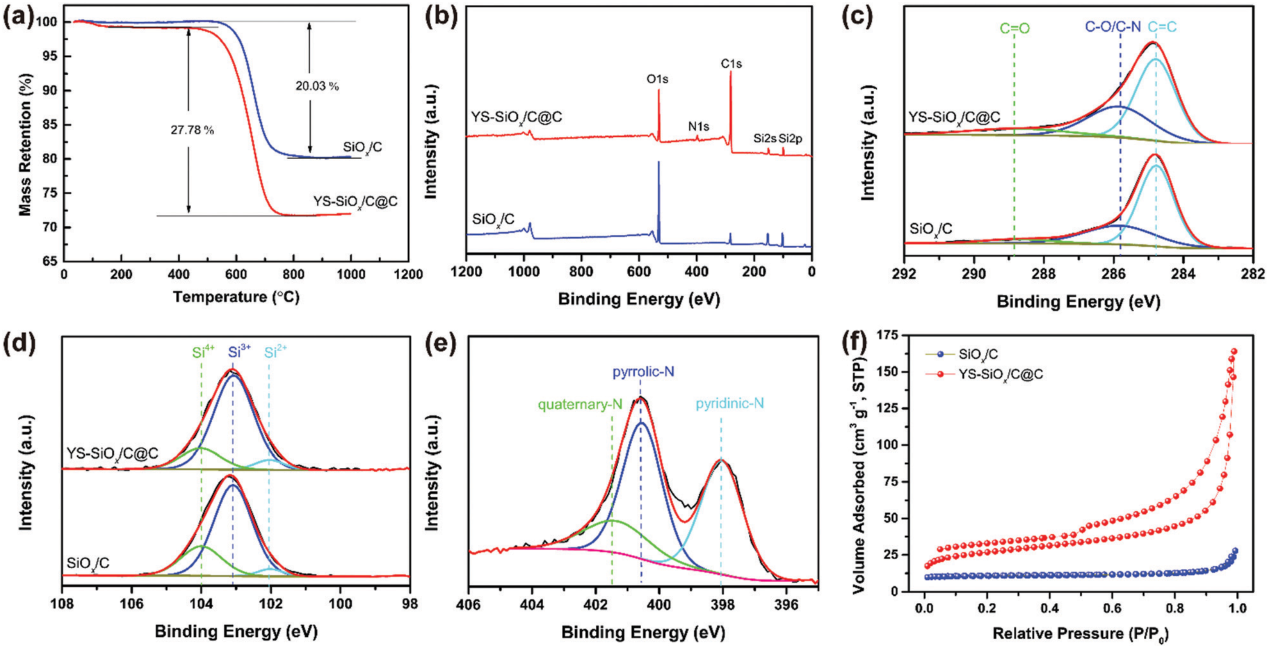

Fig. 4 TGA curves (a) of YS-SiO_x/C@C and SiO_x/C, XPS survey spectra (b), high-resolution C1s (c) and Si2p (d) spectra of YS-SiO_x/C@C and SiO_x/C, N1s (e) spectrum of YS-SiO_x/C@C, and N_2 adsorption/desorption isotherms (f) of YS-SiO_x/C@C and SiO_x/C.

SiO_x/C is 20.03 wt%, which is derived from the vinyl group. YS-SiO_x/C@C presents a higher carbon content of 27.78 wt%.

XPS spectra of the samples are provided in Fig. 4b–e. The YS-SiO_x/C@C composite presents an obvious N1s peak in the survey spectrum due to the N-doping in the carbon shell (Fig. 4b). The C1s spectra for both samples (Fig. 4c) present three components at 284.78, 285.83, and 288.89 eV, which are attributed to C═C, C–O/C–N, and C═O bonds, respectively.[37] Compared to SiO_x/C, YS-SiO_x/C@C shows a stronger C–O/C–N component (33.35% *vs.* 28.25% as a ratio) owing to the N doping. The Si2p spectra (Fig. 4d) of both samples show three components at 102.03, 103.06, and 104.01 eV, corresponding to the Si^{2+}, Si^{3+} and Si^{4+} species.[38,39] The average valence state of Si in YS-SiO_x/C@C is calculated to be ~3.12, which agrees well with our previous report.[40] In the N1s spectrum (Fig. 4e), the peaks centered at 398.1, 400.6, and 401.4 eV correspond to pyridinic N, pyrrolic N, and quaternary N.[37] As previously reported, the XPS results indicate that the N atoms in the pentagonal ring of PPy are transformed into pyridinic and quaternary N during the carbonization process.[41] A high content of pyridinic N and quaternary N is beneficial for improving the electrical conductivity and accelerating the ion diffusion, thus leading to enhanced electrochemical performance.[41,42]

The functional groups of organosilica@void@PPy and YS-SiO_x/C@C are analyzed by FT-IR (Fig. S3, ESI†). The band at 2934 cm^{-1} of organosilica@void@PPy is related to the stretching vibration of $=CH_x$ in the vinyl group of organosilica.[43] The strong band at 1080 cm^{-1} in YS-SiO_x/C@C is ascribed to the Si–O–Si stretching vibration, which splits into two peaks (1032 and 1130 cm^{-1}) in organosilica@void@PPy. The peaks centered at 1698, 1554, and 926 cm^{-1} can be ascribed to the C–N bond, C–C stretching, and out-of-plane deformation vibration of C–H on the pyrrole ring.[34,41] After carbonization, the peaks of PPy disappear and a weak peak located at 1620 cm^{-1} can be attributed to the C–N bond in the YS-SiO_x/C@C composite.[39] Besides, the organic groups of $=CH_x$ disappear, suggesting successful transformation of the organic groups into amorphous carbon during carbonization.

With the unique yolk@shell structure, YS-SiO_x/C@C shows a relatively high BET surface area of 119 m^2 g^{-1} as calculated from the N_2 sorption results (Fig. 4f). By contrast, the specific surface area of SiO_x/C microspheres derived from organosilica is only 9 m^2 g^{-1}. The hollow void and porous carbon shell of YS-SiO_x/C@C are able to effectively improve the contact between electrochemically active SiO_x and the electrolyte, speeding up the ion transport.

The CV profiles and selected charge–discharge curves of YS-SiO_x/C@C are displayed in Fig. 5a and b. The initial cathodic scan displays a peak at around 1.40 V, which can be attributed to the formation of an SEI film and formation of lithium silicates, Si, and Li_2O from SiO_x.[17,18] In subsequent cycles, the above-mentioned cathodic peak disappears. The cathodic peak below 0.32 V is caused by the reaction of Si with Li. The anodic peak at 0.42 V is associated with the dealloying of Li_xSi. The overlapping curves demonstrate good reversibility of the alloying/de-alloying reaction.

The initial discharge capacity of YS-SiO_x/C@C reaches 1443 mA h g^{-1} and the initial coulombic efficiency (ICE) is 54.4%. The ICE of YS-SiO_x/C@C is lower than that of SiO_x/C (58.6%) owing to its higher specific surface area, which leads to more SEI formation (Fig. 5b). The irreversible capacity loss for both samples is caused by the SEI layer formation and conversion reaction of SiO_x. Fig. 5c presents the cycling properties of the samples at 100 mA g^{-1}. Although SiO_x/C displays a high

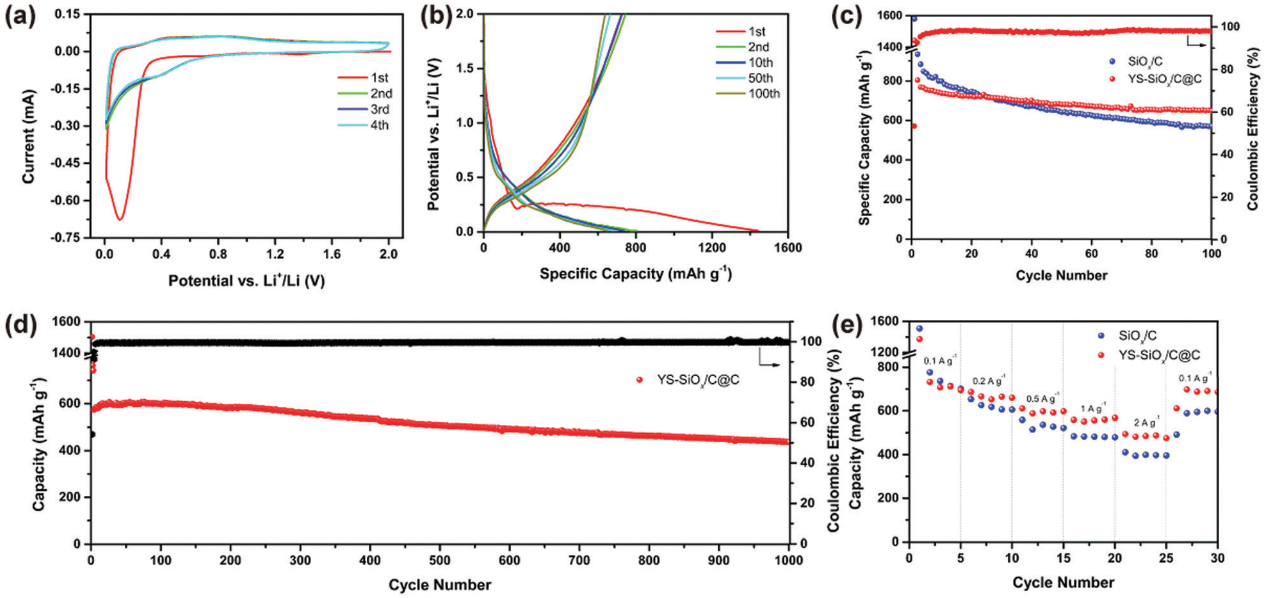

Fig. 5 CV curves (a) of YS-SiO_x/C@C in the potential range of 0.01–2.0 V *vs.* Li^+/Li at 0.1 mV s^{-1}, selected galvanostatic charge–discharge profiles (b) of YS-SiO_x/C@C at 100 mA g^{-1}, cycling performances (c) of YS-SiO_x/C@C and SiO_x/C at 100 mA g^{-1}, long-term cycling performances (d) of YS-SiO_x/C@C at 500 mA g^{-1}, and rate performances (e) of YS-SiO_x/C@C and SiO_x/C.

capacity of 933 mA h g^{-1} in the 2nd discharge, the capacity fades to 560 mA h g^{-1} after 100 cycles. Especially, the capacity decay is very serious in the first 20 cycles. In contrast, the discharge capacity of YS-SiO_x/C@C decreases slightly from 804 to 648 mA h g^{-1} during the 2nd to 100th cycle and the capacity retention reaches 81%. The average coulombic efficiency of YS-SiO_x/C@C at 100 mA g^{-1} is 97.8%.

The long-term cyclability of YS-SiO_x/C@C at 500 mA g^{-1} is also recorded to confirm the merits of the yolk@shell structure. As exhibited in Fig. 5d, YS-SiO_x/C@C still shows outstanding long-term cyclability. It delivers a reversible capacity of ~577 mA h g^{-1} and demonstrates a remarkable capacity retention of 76.4% after 1000 cycles at 500 mA g^{-1}. The average coulombic efficiency at 500 mA g^{-1} reaches 99.6%, much higher than that at low current density. The cycling performances at a higher current density of 2000 mA h g^{-1} are provided in Fig. S4 (ESI†). At such a high current density, YS-SiO_x/C@C demonstrates a capacity retention of 89% from the 4th to 100th cycle, while that of SiO_x/C is only 62%. The improved cyclability is associated with the existence of hollow voids for volume variation accommodation and the formation of a more stable SEI.

SiO_x/C@C also demonstrates excellent rate capability. Even at 2000 mA g^{-1}, a high specific capacity of ~494 mA h g^{-1} is achieved (Fig. 5e). When the current density is returned to 100 mA g^{-1}, the capacity increases to a high value of ~697 mA h g^{-1}. In contrast, the capacity of SiO_x/C at 2000 mA g^{-1} is only ~396 mA h g^{-1}. To better highlight the merits of YS-SiO_x/C@C, the electrochemical performance of YS-SiO_x/C@C is compared with state-of-the-art SiO_x-based anode materials in Table S1 (ESI†). YS-SiO_x/C@C demonstrates comparable lithium storage performances in terms of capacity and cyclability.

EIS was also conducted. The Nyquist plots of the samples are provided in Fig. S5 (ESI†). The low-frequency straight line stands for the Warburg impedance (W), and its slope reflects the diffusivity of Li^+ in the electrode material. The high-frequency semi-circle corresponds to the charge-transfer resistance (R_{ct}). According to the result, YS-SiO_x/C@C exhibits a significantly smaller R_{ct} and slightly lower W than SiO_x/C, suggesting that the introduction of the yolk@shell structure plays a vital role in improving the electrical conductivity and electrode kinetics.

For high-capacity anode materials such as SiO_x, the large volume fluctuation and the associated poor structural integrity are always a problem. To demonstrate that the enhanced cycling stability of YS-SiO_x/C@C results from the volume expansion buffering ability of the yolk@shell structure, TEM images after 100 cycles at 2000 mA h g^{-1} are collected (in the lithiated state). When compared to pristine YS-SiO_x/C@C, two obvious changes can be observed in Fig. 6. First, the thickness of the N-doped carbon shell increases from 30 to 50 nm, which may be caused by the lithiation induced volume expansion and formation of the SEI layer on the surface of the protective carbon shell. Second, the size of the yolk increases from 300 to 360 nm and it occupies almost all the hollow cavity in the lithiated state. The whole hollow cavity can be fully utilized during the lithiation and is beneficial for achieving high volumetric capacity.[30] Despite these changes, the yolk@shell structure can still be maintained after 100 cycles, demonstrating excellent structural stability. The above results clearly demonstrate that the yolk@shell structure of YS-SiO_x/C@C is able to buffer the volume variation during cycling and improve the structural integrity, thus resulting in enhanced cycling stability.

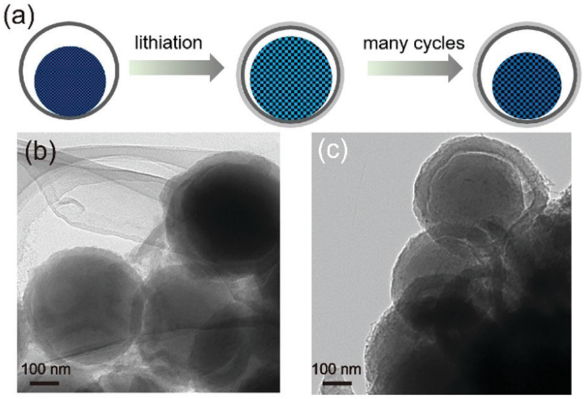

Fig. 6 Schematic illustration (a) showing the structure evolution of YS-SiO_x/C@C during cycling, and TEM images (b and c) of YS-SiO_x/C@C after 100 cycles at 2000 mA g^{-1}.

To further verify the potential practical applications of YS-SiO_x/C@C in LIBs, full-cells are assembled. The electrochemical performances of $LiFePO_4$ and YS-SiO_x/C@C//$LiFePO_4$ full-cells are displayed in Fig. S6 (ESI†). The YS-SiO_x/C@C sample was pre-lithiated in half-cells to avoid the irreversible Li^+ consumption in the initial cycles.[44,45] Relatively flat discharge plateaus can be observed between 2.0 and 3.3 V in the charge–discharge profiles. The cycling stability of the full cell is tested at 0.1C for 100 cycles between 2.2 and 4.0 V. Based on the mass of $LiFePO_4$, the YS-SiO_x/C@C//$LiFePO_4$ full cell delivers a capacity of 160 mA h g^{-1} at 0.1C and a capacity retention of 90.2% after 50 cycles, which is similar to the performance of $LiFePO_4$ in half cells.

Conclusion

In summary, SiO_x/C@N-doped carbon yolk@shell microspheres have been constructed based on a dopamine sacrificial layer mediated route. The rationally designed yolk@shell structure buffers the large volume expansion of SiO_x/C, resulting in significantly enhanced structural integrity. The obtained YS-SiO_x/C@C composite delivers high lithium storage capacity with excellent cyclability. The obtained YS-SiO_x/C@C composite displays a remarkable capacity retention of 76.4% after 1000 cycles at 500 mA g^{-1}. It is anticipated that the polydopamine-mediated selective etching strategy introduced in this work can be generalized to the construction of other yolk@shell structures for lithium storage.

Conflicts of interest

The authors declare no conflicts of interest.

Acknowledgements

This work was supported by the National Key Research and Development Program of China (2018YFB0104200), National Postdoctoral Program for Innovative Talents (BX20190258) and State Key Laboratory of Powder Metallurgy, Central South University, Changsha, China.

References

1 Y. M. Chiang, Building a better battery, *Science*, 2010, **330**, 1485–1486.
2 S. Choi, T. Kwon, A. Coskun and J. W. Choi, Highly elastic binders integrating polyrotaxanes for silicon microparticle anodes in lithium ion batteries, *Science*, 2017, **357**, 279–283.
3 X. Zuo, J. Zhu, P. Müller-Buschbaum and Y. J. Cheng, Silicon based lithium-ion battery anodes: A chronicle perspective review, *Nano Energy*, 2017, **31**, 113–143.
4 Y. Jin, B. Zhu, Z. Lu, N. Liu and J. Zhu, Challenges and recent progress in the development of Si anodes for lithium-ion battery, *Adv. Energy Mater.*, 2017, **7**, 1700715.
5 J. Yang, Y. Wang, W. Li, L. Wang, Y. Fan, W. Jiang, W. Luo, Y. Wang, B. Kong and C. Selomulya, Amorphous TiO_2 Shells: A Vital Elastic Buffering Layer on Silicon Nanoparticles for High-Performance and Safe Lithium Storage, *Adv. Mater.*, 2017, **29**, 1700523.
6 J. Wang, L. Liao, H. R. Lee, F. Shi, W. Huang, J. Zhao, A. Pei, J. Tang, X. Zheng, W. Chen and Y. Cui, Surface-engineered mesoporous silicon microparticles as high-coulombic-efficiency anodes for lithium-ion batteries, *Nano Energy*, 2019, **61**, 404–410.
7 Z. Yi, N. Lin, Y. Zhao, W. Wang, Y. Qian, Y. Zhu and Y. Qian, A flexible micro/nanostructured Si microsphere cross-linked by highly-elastic carbon nanotubes toward enhanced lithium ion battery anodes, *Energy Storage Mater.*, 2019, **17**, 93–100.
8 L. C. Loaiza, L. Monconduit and V. Seznec, Si and Ge-Based Anode Materials for Li^-, Na^-, and K^- Ion Batteries: A Perspective from Structure to Electrochemical Mechanism, *Small*, 2020, **16**, 1905260.
9 J. Sung, J. Ma, S. H. Choi, J. Hong, N. Kim, S. Chae, Y. Son, S. Y. Kim and J. Cho, Fabrication of Lamellar Nanosphere Structure for Effective Stress-Management in Large-Volume-Variation Anodes of High-Energy Lithium-Ion Batteries, *Adv. Mater.*, 2019, **31**, 1900970.
10 B. Chen, L. Zu, Y. Liu, R. Meng, Y. Feng, C. Peng, F. Zhu, T. Hao, J. Ru, Y. Wang and J. Yang, A Space-Confined Atom-Cluster Catalytic Strategy for Direct Superassembly of Silicon Nanodots⊂Carbon Frameworks for Lithium-ion Batteries, *Angew. Chem., Int. Ed.*, 2020, **132**, 3161–3166.
11 H. Wang, J. Fu, C. Wang, J. Wang, A. Yang, C. Li, Q. Sun, Y. Cui and H. Li, A binder-free high silicon content flexible anode for Li-ion batteries, *Energy Environ. Sci.*, 2020, **13**, 848–858.
12 F. Zhang, G. Zhu, K. Wang, X. Qian, Y. Zhao, W. Luo and J. Yang, Boosting the initial coulombic efficiency in silicon anodes through interfacial incorporation of metal nanocrystals, *J. Mater. Chem. A*, 2019, **7**, 17426–17434.
13 J. Wang, L. Liao, Y. Li, J. Zhao, F. Shi, K. Yan, A. Pei, G. Chen, G. Li, Z. Lu and Y. Cui, Shell-protective secondary silicon

nanostructures as pressure-resistant high-volumetric-capacity anodes for lithium-ion batteries, *Nano Lett.*, 2018, **18**, 7060–7065.

14 J. Lee, J. Moon, S. A. Han, J. Kim, V. Malgras, Y. U. Heo, H. Kim, S. M. Lee, H. K. Liu, S. X. Dou, Y. Yamauchi, M. S. Park and J. H. Kim, Everlasting Living and Breathing Gyroid 3D Network in Si@SiO_x/C Nanoarchitecture for Lithium Ion Battery, *ACS Nano*, 2019, **13**, 9607–9619.

15 L. Zhang, J. Deng, L. Liu, W. Si, S. Oswald, L. Xi, M. Kundu, G. Ma, T. Gemming and S. Baunack, Hierarchically designed SiO_x/SiO_y bilayer nanomembranes as stable anodes for lithium ion batteries, *Adv. Mater.*, 2014, **26**, 4527–4532.

16 Q. Xu, J. K. Sun, Y. X. Yin and Y. G. Guo, Facile Synthesis of Blocky SiO_x/C with Graphite-Like Structure for High-Performance Lithium-Ion Battery Anodes, *Adv. Funct. Mater.*, 2018, **28**, 1705235.

17 J. Zhang, C. Zhang, Z. Liu, J. Zheng, Y. Zuo, C. Xue, C. Li and B. Cheng, High-performance ball-milled SiO_x anodes for lithium ion batteries, *J. Power Sources*, 2017, **339**, 86–92.

18 Z. Liu, Q. Yu, Y. Zhao, R. He, M. Xu, S. Feng, S. Li, L. Zhou and L. Mai, Silicon oxides: a promising family of anode materials for lithium-ion batteries, *Chem. Soc. Rev.*, 2019, **48**, 285–309.

19 W. Guo, X. Yan, F. Hou, L. Wen, Y. Dai, D. Yang, X. Jiang, J. Liu, J. Liang and S. X. Dou, Flexible and free-standing SiO_x/CNT composite films for high capacity and durable lithium ion batteries, *Carbon*, 2019, **152**, 888–897.

20 G. Zhu, F. Zhang, X. Li, W. Luo, L. Li, H. Zhang, L. Wang, Y. Wang, W. Jiang and H. K. Liu, Engineering the distribution of carbon in silicon oxide nanospheres at atomic level for highly stable anodes, *Angew. Chem., Int. Ed.*, 2019, **58**, 6669–6673.

21 J. Wang, H. Tang, L. Zhang, H. Ren, R. Yu, Q. Jin, J. Qi, D. Mao, M. Yang, Y. Wang, P. Liu, Y. Zhang, Y. Wen, L. Gu, G. Ma, Z. Su, Z. Tang, H. Zhao and D. Wang, Multi-shelled metal oxides prepared via an anion-adsorption mechanism for lithium-ion batteries, *Nat. Energy*, 2016, **1**, 1–9.

22 C. Wu, X. Tong, Y. Ai, D.-S. Liu, P. Yu, J. Wu and Z. M. Wang, A review: enhanced anodes of li/Na-ion batteries based on yolk–shell structured nanomaterials, *Nano-Micro Lett.*, 2018, **10**, 40.

23 J. Wang, H. Tang, H. Wang, R. Yu and D. Wang, Multi-shelled hollow micro-/nanostructures: promising platforms for lithium-ion batteries, *Mater. Chem. Front.*, 2017, **1**, 414–430.

24 B. Zhang, Y. Li, C. Yang and Z. Deng, Yolk-shell manganese oxide nanostructures for lithium-ion battery anodes, *Chin. Sci. Bull.*, 2019, **64**, 3371–3377.

25 F. Xie, L. Zhang, C. Ye, M. Jaroniec and S. Z. Qiao, The Application of Hollow Structured Anodes for Sodium-Ion Batteries: From Simple to Complex Systems, *Adv. Mater.*, 2019, **31**, 1800492.

26 J. Wang, N. Yang, H. Tang, Z. Dong, Q. Jin, M. Yang, D. Kisailus, H. Zhao, Z. Tang and D. Wang, Accurate control of multishelled Co_3O_4 hollow microspheres as high-performance anode materials in lithium-ion batteries, *Angew. Chem., Int. Ed.*, 2013, **52**, 6417–6420.

27 N. Liu, Z. Lu, J. Zhao, M. T. McDowell, H. W. Lee, W. Zhao and Y. Cui, A pomegranate-inspired nanoscale design for large-volume-change lithium battery anodes, *Nat. Nanotechnol.*, 2014, **9**, 187.

28 Z. Liu, X. Y. Yu, X. W. Lou and U. Paik, Sb@C coaxial nanotubes as a superior long-life and high-rate anode for sodium ion batteries, *Energy Environ. Sci.*, 2016, **9**, 2314–2318.

29 H. Zhang, X. Huang, O. Noonan, L. Zhou and C. Yu, Tailored Yolk-Shell Sn@C Nanoboxes for High-Performance Lithium Storage, *Adv. Funct. Mater.*, 2017, **27**, 1606023.

30 H. Zhang, L. Zhou, O. Noonan, D. J. Martin, A. K. Whittaker and C. Yu, Tailoring the Void Size of Iron Oxide@Carbon Yolk–Shell Structure for Optimized Lithium Storage, *Adv. Funct. Mater.*, 2014, **24**, 4337–4342.

31 Y. Liu, K. Ai and L. Lu, Polydopamine and its derivative materials: synthesis and promising applications in energy, environmental, and biomedical fields, *Chem. Rev.*, 2014, **114**, 5057–5115.

32 H. A. Lee, Y. Ma, F. Zhou, S. Hong and H. Lee, Material-independent surface chemistry beyond polydopamine coating, *Acc. Chem. Res.*, 2019, **52**, 704–713.

33 H. Lee, S. M. Dellatore, W. M. Miller and P. B. Messersmith, Mussel inspired surface chemistry for multifunctional coatings, *Science*, 2007, **318**, 426–430.

34 Z. Liu, J. Li, L. Chen, H. Yu, F. Zeng and Y. Wang, Synchronous synthesis/modification of multifunctional hollow silica nanospheres through selective etching and application in catalysis, *Colloids Surf., A*, 2016, **509**, 648–655.

35 Q. Xu, J. K. Sun, Z. L. Yu, Y. X. Yin, S. Xin, S. H. Yu and Y. G. Guo, SiO_x Encapsulated in Graphene Bubble Film: An Ultrastable Li-Ion Battery Anode, *Adv. Funct. Mater.*, 2018, **30**, 1707430.

36 M. Han and J. Yu, Subnanoscopically and homogeneously dispersed SiO_x/C composite spheres for high-performance lithium ion battery anodes, *J. Power Sources*, 2019, **414**, 435–443.

37 L. Wu, J. Zheng, L. Wang, X. Xiong, Y. Shao, G. Wang, J.-H. Wang, S. Zhong and M. Wu, PPy-encapsulated SnS_2 Nanosheets Stabilized by Defects on a TiO_2 Support as a Durable Anode Material for Lithium-Ion Batteries, *Angew. Chem., Int. Ed.*, 2019, **58**, 811–815.

38 Z. Li, H. Zhao, P. Lv, Z. Zhang, Y. Zhang, Z. Du, Y. Teng, L. Zhao and Z. Zhu, Watermelon-Like Structured SiO_x-TiO_2@C Nanocomposite as a High-Performance Lithium-Ion Battery Anode, *Adv. Funct. Mater.*, 2018, **28**, 1605711.

39 Y. Ren and M. Li, Facile synthesis of SiO_x@C composite nanorods as anodes for lithium ion batteries with excellent electrochemical performance, *J. Power Sources*, 2016, **306**, 459–466.

40 Z. Liu, D. Guan, Q. Yu, L. Xu, Z. Zhuang, T. Zhu, D. Zhao, L. Zhou and L. Mai, Monodisperse and homogeneous SiO_xC microspheres: A promising high-capacity and durable anode material for lithium-ion batteries, *Energy Storage Mater.*, 2018, **13**, 112–118.

41 W. Luo, F. Li, J. J. Gaumet, P. Magri, S. Diliberto, L. Zhou and L. Mai, Bottom-Up Confined Synthesis of Nanorod-in-Nanotube Structured Sb@N-C for Durable Lithium and Sodium Storage, *Adv. Energy Mater.*, 2018, **8**, 1703237.

42 W. Shen, C. Wang, Q. Xu, H. Liu and Y. Wang, Nitrogen-doping-induced defects of a carbon coating layer facilitate Na-storage in electrode materials, *Adv. Energy Mater.*, 2015, **5**, 1400982.

43 H. J. Kim, S. Choi, S. J. Lee, M. W. Seo, J. G. Lee, E. Deniz, Y. J. Lee, E. K. Kim and J. W. Choi, Controlled prelithiation of silicon monoxide for high performance lithium-ion rechargeable full cells, *Nano Lett.*, 2016, **16**, 282–288.

44 P. Nie, Z. Le, G. Chen, D. Liu, X. Liu, H. B. Wu, P. Xu, X. Li, F. Liu, L. Chang, X. Zhang and Y. Lu, Graphene caging silicon particles for high-performance lithium-ion batteries, *Small*, 2018, **14**, 1800635.

45 W. He, Y. Liang, H. Tian, S. Zhang, Z. Meng and W.-Q. Han, A facile in situ synthesis of nanocrystal-FeSi-embedded Si/SiO$_x$ anode for long-cycle-life lithium ion batteries, *Energy Storage Mater.*, 2017, **8**, 119–126.